IOP Publishing Measurement Science and Technology
Meas. Sci. Technol. **31** (2020) 055901 (14pp) https://doi.org/10.1088/1361-6501/ab5092

Evaluation of parasitic resistance in voltage-driven electrical resistance tomography

Chao Wang, Qingqing Cao, Yuxiang Chen, Huaxiang Wang and Ziqiang Cui

Tianjin Key Laboratory of Process Measurement and Control, School of Electrical and Information Engineering, Tianjin University, Tianjin 300072, People's Republic of China

E-mail: cuiziqiang@tju.edu.cn

Received 22 July 2019, revised 30 September 2019
Accepted for publication 23 October 2019
Published 6 February 2020

Abstract

Electrical resistance tomography (ERT) is an effective method for monitoring electrical conductivity distribution in the field using boundary measurement information. In applications with a large pipe diameter and large load variation, voltage-driven ERT (ERTv) can overcome the limitations of current-driven ERT (ERTc). A voltage source is used in ERTv to apply an excitation signal to the electrode, and can provide a large output signal. Meanwhile, saturation will not occur when the load of the field shows large fluctuations. However, the main disadvantage of an ERTv system is that the parasitic resistance in the system has an influence on the measurement results which cannot be ignored. The existence of parasitic resistance can cause measurement errors and reduce the reliability of ERTv systems. In this paper, the influence of parasitic resistance was evaluated and the trend of variation of this effect with different background conductivities was studied. The index k_r was defined to find the relationship between parasitic resistance and background conductivity. When $k_r \leqslant 3 \times 10^{-2}$, the reconstructed image can better reflect the actual conductivity distribution. At the same time, the applicable background conductivity range of the system can be acquired according to k_r, when the value of parasitic resistance in the system is known in advance.

Keywords: electrical resistance tomography, voltage excitation, conductivity distribution, parasitic resistance, reconstructed image

(Some figures may appear in colour only in the online journal)

1. Introduction

Electrical resistance tomography (ERT) is an effective tool for online visualization of aqueous-based multi-phase flows. It has the advantages of being non-radioactive and non-intrusive with a rapid response and is economical for extended use. ERT can be applied in a variety of industrial processes [1–4].

Generally, an ERT system employs a current source and strategy for trans-impedance measurement, denoted as current-driven ERT (ERTc) [5–7]. ERTc can be implemented with different exciting modes, including the neighboring method, cross method and opposite method [8–10]. ERTc systems are immune to parasitic resistance [11], namely contact impedance between the electrodes and liquid, the ON-resistance of analog switches and the resistance of the wire. However, the performance of an ERTc system is greatly affected by the quality of current source [12]. It is usually difficult to implement an ideal current source, i.e. one that can maintain a steady current output for a fast-changing load [13]. Secondly, ERTc measurements are very likely to be saturated when performed in a low-conductivity fluid. Thirdly, the small-sized electrodes that are widely adopted in ERTc sensors can cause significant fringe effects and image distortion [14, 15].

In order to improve the limitations of ERT, Jia *et al* proposed an ERT system using a voltage source [16]. In this

system, the maximum current output could be nearly four times greater than with an ERTc system, but the saturation phenomenon remained. Frias and Yang then proposed the voltage-driven ERT (ERTv) system that utilizes a voltage source and current-sensing circuit to achieve impedance measurement [17]. In this system, an AC voltage signal is applied to one electrode and the currents flowing out of the other electrodes are measured—this was actually developed from the AC-based electrical capacitance tomography (ECT) system. Yang and colleagues then compared the ERTv system with the ECT system [18]. In this research, the ERTv system was good for measuring a high-moisture gas–solid flow and a gas–liquid flow with low or moderate background conductivity. Considering the advantages of the ERTv system, Cui *et al* developed a twin-plane system using ERTv with the aim of avoiding the measurement saturation phenomenon that exists in ERTc systems [19]. In addition, ERTv can achieve more independent measurements than ERTc for a sensor with the same number of electrodes [20, 21]. These advantages contribute to the improved image quality of ERTv systems [22].

ERTv measurement systems have been rarely employed before. This is because most ERT systems are applied in aqueous-based processes, wherein high-conductivity chemical solutions can be expected [23]. In these cases, inter-electrode resistances are very low [8–10]. In other cases, however, this condition cannot be satisfied [17–19]. The load of the signal source can be tens of kilohms and the output signal of the current source can be easily saturated. Therefore, the ERTv system has been proposed to handle this large resistance load. In fact, ERTv systems have recently undergone rapid development and are considered suitable for many applications, for example processes in large-diameter vessels.

In ERTv systems, the parasitic resistance that shunts with the measured impedance constitutes a major drawback, and the presence of parasitic resistance prevents the excitation voltage from being applied directly to the measured medium. When the parasitic resistance is comparable with the measured resistance its influence becomes even more significant.

In order to evaluate the influence of parasitic resistance, Yang *et al* designed a four-terminal sensor for ERTv [24]. In this sensor, a rectangular plate with a large area was used as the excitation plate, and a circular point electrode with a small area was removed from the plate as the detection electrode. At the same time, the voltage at both ends of the measured object field was obtained. The conductance of the channel was calculated from these two parameters. With this method, the partial voltage generated by the contact impedance in series can be ignored. This reduces the impact of contact impedance to a great extent. In addition, Rodriguez-Frias and Yang proposed a new electrode structure, extending the point electrodes to a connected rectangular box [25]. In this way, the average voltage within this rectangular area was calculated instead of the voltage at a specific point. This method can reduce randomness and ensure that an average voltage can be measured.

These sensor structures are an effective way to reduce the effect of contact impedance. However, there has been little research on other parasitic resistances and the influence of parasitic resistance on measurement under different background conductivities has rarely been reported. From this perspective, this paper focuses on the influence of parasitic resistance on the measurement and imaging of ERTv with background conductivity changes. Using an ERTv system, the measurements and the sensitivity distribution of the system with parasitic resistance were first obtained. Then, a study for different values of parasitic resistance was performed to find out how measurement results vary under different background conductivities. With this information, the range of background conductivity applicable to the system can be determined with fixed parasitic resistance. Finally, experiments were done to verify the simulation results.

2. Method

2.1. Sensing strategies

As mentioned above, the ERTv system is developed from the ECT system. An AC voltage signal is applied and the currents flowing out of the other electrodes are collected to calculate the conductances between electrodes. In order to obtain the conductivity distribution of the sensing field, a mathematical model of ERTv needs to be established. The sensing field is analyzed in a two-dimensional plane and the fringe effect caused by finite electrode length is neglected. Usually the electrical field can be regarded as a quasi-static electric field, which is determined by Maxwell function as follows [26, 27]:

$$\begin{cases} \nabla \times H = J = \sigma E \\ \nabla \times E = -\frac{\partial B}{\partial t} = -\mu \frac{\partial H}{\partial t} \\ \nabla \cdot B = 0 \\ \nabla \cdot D = 0 \end{cases} \tag{1}$$

where H is the magnetic field intensity, J is the electric current density, E is the electric field intensity, B is the magnetic induction intensity, D is the electric flux density, σ is the conductivity and μ is the magnetoconductivity.

The quasi-static electric field follows the law of static fields. It can be calculated by

$$\nabla^2 \phi = 0. \tag{2}$$

Under these conditions, the mathematical model of ERTv can be described by

$$\begin{cases} \nabla^2 \phi(x, y) = 0, & (x, y) \in \Omega \\ \phi_i(x, y) = U_e, & (x, y) \in \Gamma_e \\ \phi_j(x, y) = 0, & (x, y) \in \Gamma_0 \end{cases} \tag{3}$$

where $\phi(x, y)$ is the potential distribution, U_e is the excitation voltage applied to the field, i and j are the indices of excitation and detection electrodes, respectively, Ω is the sensing field, Γ_e is the excitation electrode and Γ_0 is the other electrodes.

Equation (3) is the mathematical model of the ERTv, and can be analyzed by the finite-element method. In this work, the simulation process is performed by COMSOL Multiphysics. The simulation area of the ERTv is meshed by triangle elements. Based on the simulation program, the potential of the element nodes can be obtained.

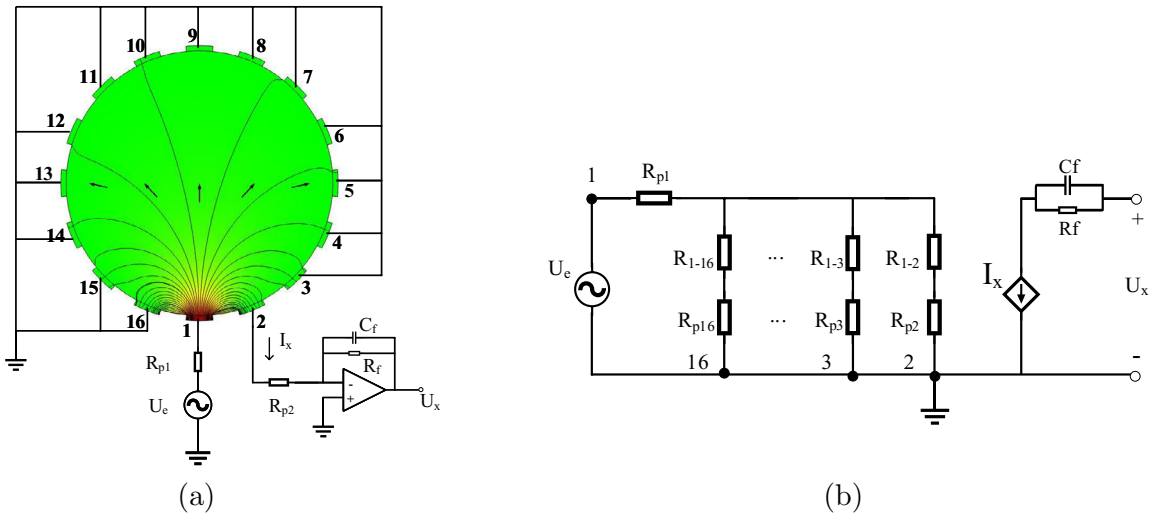

Figure 1. Sensing strategies of an ERTv system: (a) potential distribution, (b) equivalent circuit diagram.

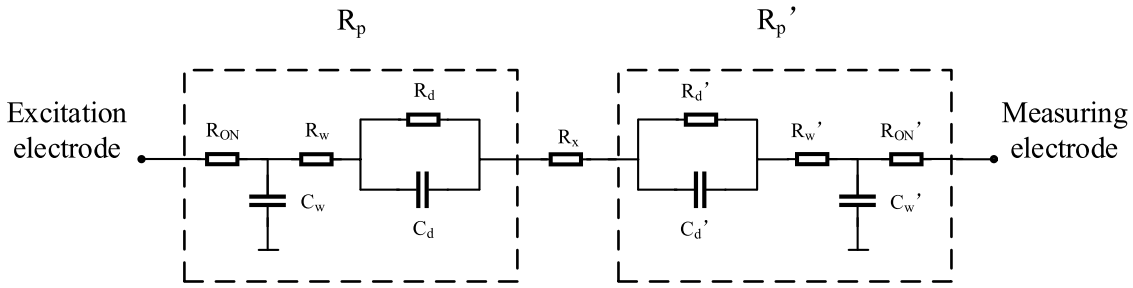

Figure 2. Equivalent circuit of parasitic resistance.

As shown in figure 1(a), a voltage signal is applied to the excitation electrode, while a measurement electrode is connected to the current sensing circuit. At the same time, the remaining electrodes are connected to ground. Figure 1(b) shows the equivalent circuit of the sensing strategies, where U_e is the excitation voltage and I_x is the measurement current. Then the conductance between the excitation electrode and the measurement electrode can be calculated by $G = I_x/U_e$

2.2. Parasitic resistance

Figure 2 shows the equivalent circuit of parasitic resistance in the measurement. Here, R_x is the resistance under test, R_p and R'_p represent the parasitic resistance in the excitation channel and measurement channel, respectively, R_{ON} is the resistance of the analog switches in each channel and R_w and C_w stand for the wire resistance and the wire capacitance respectively. R_d and C_d in parallel represent the contact impedance, in which R_d is the charge transfer resistance and C_d is the double-layer capacitance [28].

In contact impedance, the capacitive reactance can be calculated by $1/jwC_d$. In ERTv, C_d is usually large due to the large area of the electrode. Under the application of a high excitation frequency, the contact impedance can be neglected.

Considering the parasitic resistance, the current that flows out of the electrode can be calculated as $I = U_e/(R_x + R_p + R'_p)$. Under the excitation of U_e, I is determined not only by the resistance of the field R_x but also by the parasitic resistances R_p and R'_p.

2.3. Image reconstruction

For ERT, the relationship between the measurements and the conductivity distribution can be approximated by a linear function [29], i.e.

$$\lambda = SG \tag{4}$$

where λ is the measurement vector, G is the conductivity distribution vector and S is the sensitivity matrix of ERT [30], formulated by

$$S_{i,j}(x,y) = -\int_{\Omega(x,y)} \frac{\nabla\varphi_i(x,y)}{U_e} \cdot \frac{\nabla\varphi_j(x,y)}{U_e} \mathrm{d}x\mathrm{d}y. \tag{5}$$

Here $S_{i,j}(x, y)$ is the sensitivity at (x, y), $\varphi_i(x, y)$ and $\varphi_j(x, y)$ are the potential distributions due to electrodes i and j, respectively, at an applied voltage U_e.

In ERTv the linear back projection (LBP) algorithm has been widely used for online image reconstruction due to its simplicity and fast speed [31]. There are also more accurate algorithms, such as regularization methods and iterative algorithms, which need more parameters [32]. To perform objective image comparisons, image reconstruction is accomplished by the LBP algorithm, which can be calculated by [33]

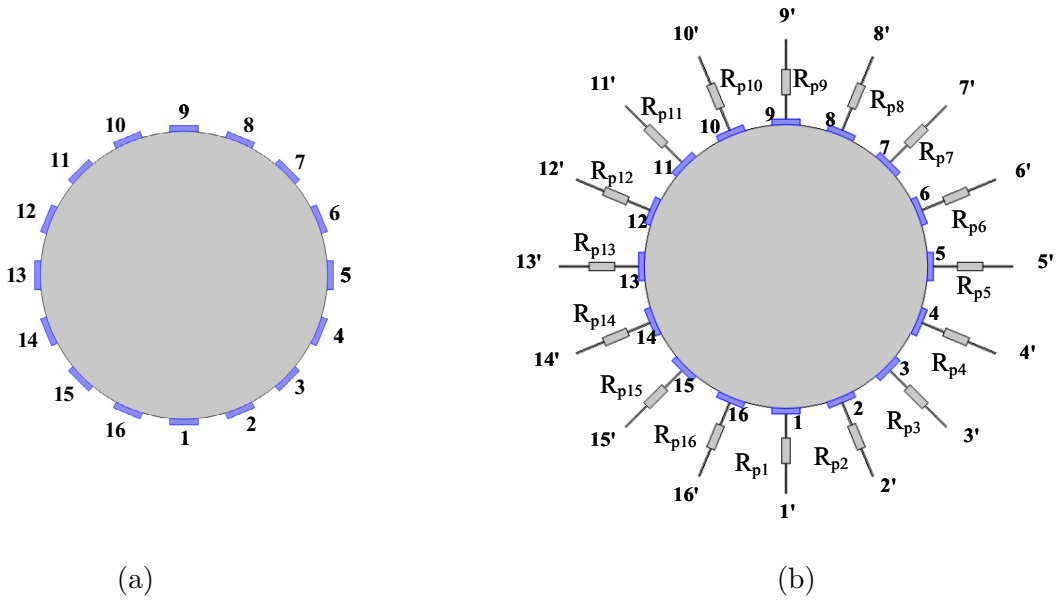

Figure 3. Simulation models of the ERTv sensors: (a) sensor without R_p, (b) sensor with R_p.

$$\hat{G} = \frac{S^T \lambda}{S^T u_\lambda} \tag{6}$$

where $\hat{G}$ is the image representing the conductivity distribution, S^T is the transpose of the sensitivity matrix and u_λ is a vector of ones with the same dimension as λ.

- diameter of sensing field: 100 mm
- total number of electrodes: 16
- width of electrode: 11 mm
- thickness of the electrode: 2 mm
- electrode material: copper
- excitation voltage: $U_e = 1\ V$.

3. Results and discussions

3.1. Numerical simulations

In order to achieve greater accuracy, the multi-physical coupling software COMSOL Multiphysics is used to build the model for the simulation experiments. Figure 3 shows the simulation models for ERTv sensors, with part (a) showing the 16-electrode ERTv sensor without considering parasitic resistances. The excitation voltage signal is directly applied to one of the electrodes and the current flowing out of each terminal is determined by calculating the line integral of normal current density on the boundaries of each measurement electrode, i.e.

$$I_x = \int_{\Gamma_m} \vec{J_n} \mathrm{d}\vec{l} \tag{7}$$

where I_x is the measurement current and $\vec{J_n}$ is the normal current density on the boundary of the measurement electrode Γ_m.

Correspondingly, figure 3(b) demonstrates the ERTv sensor with parasitic resistances. The resistances R_{pi} are the parasitic resistances. Instead of directly applying an excitation signal to the electrodes, i.e. terminals 1–16, the excitation voltage is applied to terminals $1'$–$16'$. The currents flowing out of the other measurement electrodes are also collected from terminals $1'$ to $16'$. The main parameters of the sensor models are as follows:

3.1.1. Forward problem. Figure 4 shows the measurement currents when the sensing field is filled with water (conductivity 1×10^{-2}S m^{-1}). It can be seen that the parasitic resistance has a significant influence on the ERTv measurement. When considering the existence of parasitic resistance, the dynamic range of the measurement currents becomes smaller.

The presence of parasitic resistance also influences the voltage between the excitation electrode and the measurement electrode, which can be calculated by

$$\Delta U_e = U_e - I_x(R_{pi} + R_{pj}) \tag{8}$$

where I_x is the measurement current and R_{pi} and R_{pj} are the parasitic resistances related to electrodes i and j, respectively.

Figure 5 shows the variation of ΔU_e in the different channels. In this paper the excitation voltage is 1V and the measurement electrodes are connected to the actual ground or measurement circuit (virtual ground), so ΔU_e of the sensor without R_p is 1V. It can be seen that ΔU_e becomes smaller when considering R_p, especially in channels 1 and 15. Here, channels 1 and 15 represent measurement electrodes 2 and 16, respectively, while 1V is applied to electrode 1. Both these channels are adjacent to excitation electrode 1. In these cases, the outflow current from the measurement electrodes are larger, which results in a greater voltage drop. Consequently, ΔU_e of these two channels is smaller than that of other channels.

The existence of parasitic resistance means that the excitation voltage cannot be applied directly to the electrodes.

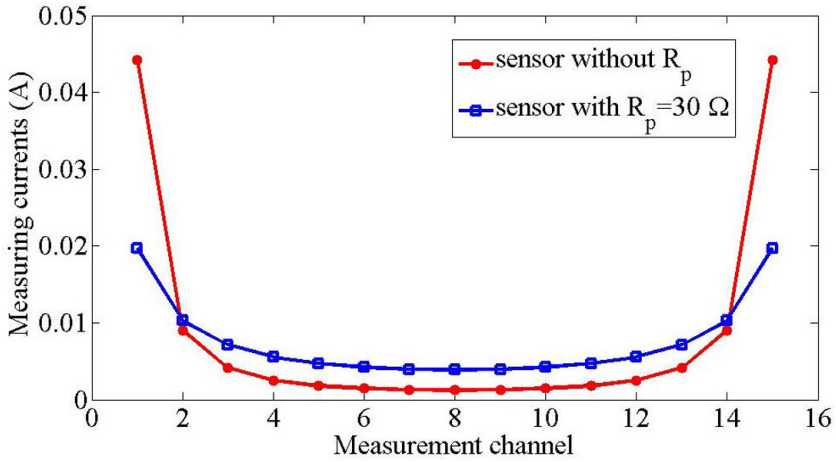

Figure 4. Comparison of the measurement currents.

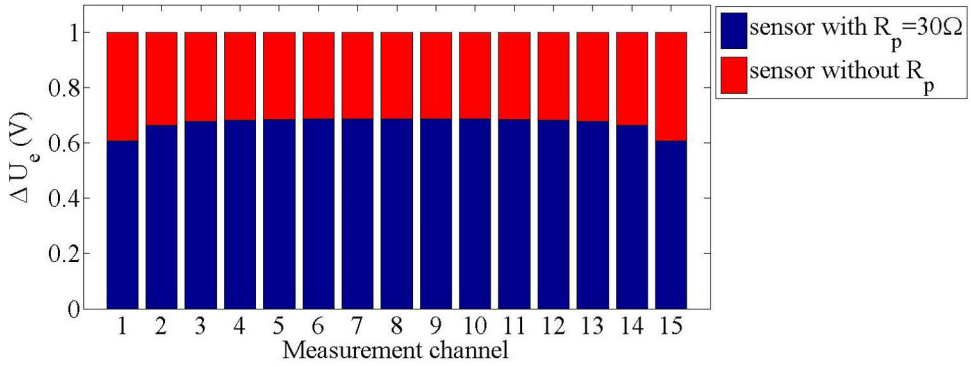

Figure 5. Voltage difference between the excitation electrode and measurement electrode.

Table 1. Sensitivity maps.

Electrode pair	1–2	1–3	1–5	1–7	1–9
Sensor without R_p $P = 0.9499$	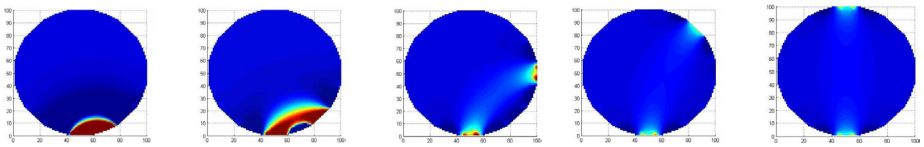				
Sensor with R_p $P = 1.5601$	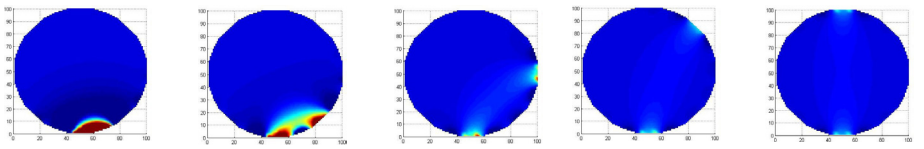				

Consequently, the voltages applied to the sensing field are usually smaller than under normal situations. The lower excitation voltage will result in a lower sensitivity in the sensing field.

3.1.2. Sensitivity map. The sensitivity is usually defined as the change in channel measurements due to conductivity perturbation within a pixel inside the sensing field. In the 16-electrode ERTv sensor, there are 120 independent measurement channels. In this research, the number of image pixels is 812. Consequently, the size of the sensitivity matrix is 120×812. In the ERTv sensor, the sensitivity distribution also depends on ΔU_e. As shown in figure 5, the voltage can be kept at ΔU_e when there is no parasitic resistance, but the situation changes when there is parasitic resistance. Thus, it is necessary to consider the specific distribution of sensitivity in the presence of parasitic resistance.

Table 1 shows the sensitivity distribution of different channels. The sensitivity distributions in each case are similar, i.e. low at the

Table 2. The trend of measurement current under different background conductivities.

R_p	Phantom 1	Phantom 2
300 Ω	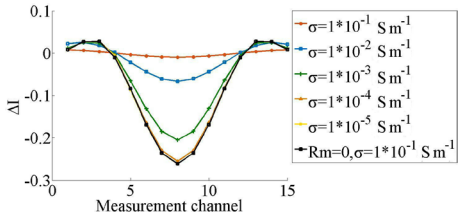	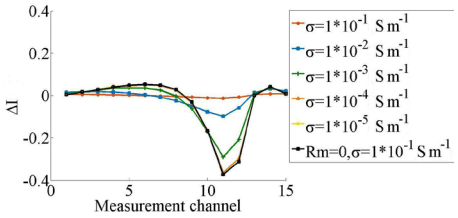
30 Ω	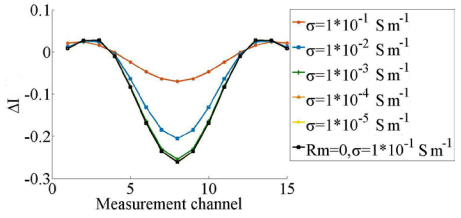	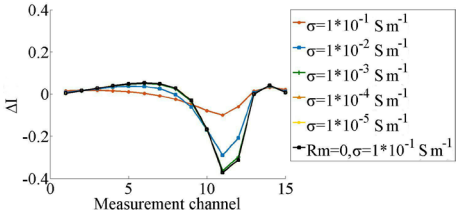
3 Ω	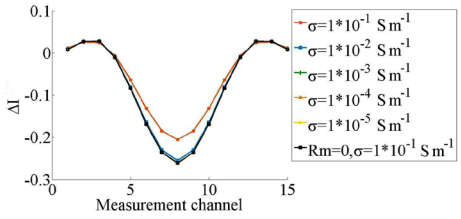	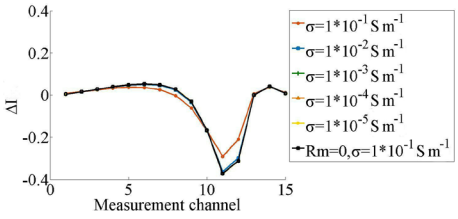
0.3 Ω	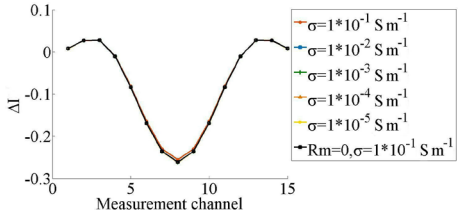	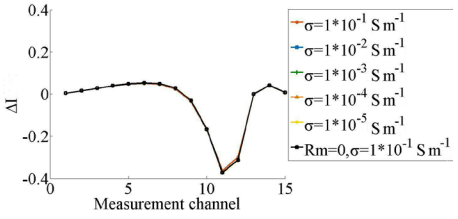

center of the field and high near the electrodes. It can be seen that the distribution under the sensor with R_p is lower than that without R_p in the center of the sensing field. In order to quantitatively evaluate the uniformity of the sensitivity matrix, a uniformity index has been proposed [34], which can be calculated by

$$P = \frac{\sum_{i=1}^{15}\sum_{j=i}^{16}|P_{i,j}|}{M} \tag{9}$$

where M is the number of independent measurements (here, for a 16-electrode system, $M = 120$). $P_{i,j}$ is the uniformity index of the sensitive field between electrodes i and j, which can be calculated by

$$\begin{cases} S_{i,j}^{\text{avg}} = \frac{1}{n}\sum_{e=1}^{n} S_{i,j}(e) \\ S_{i,j}^{\text{dev}} = \left(\frac{1}{n-1}\sum_{e=1}^{n} S_{i,j}(e) - S_{i,j}^{\text{avg}\,2}\right)^{1/2} \\ P_{i,j} = \frac{S_{i,j}^{\text{dev}}}{S_{i,j}^{\text{avg}}} \end{cases} \tag{10}$$

where $S_{i,j}^{\text{avg}}$ and $S_{i,j}^{\text{dev}}$ are the mean and standard deviation of the sensitivity matrix, respectively. i and j represent the number of excitation electrodes and measurement electrodes, respectively, n is the total number of pixels in the sensitive field and e is one of the pixels.

A smaller uniformity index P usually suggests better uniformity in the distribution of the sensitive field.

In this system, the value of index P is 0.9499 when there is no parasitic resistance. In contrast, the value of index P rises to 1.5601 for the sensor with $R_p = 30\ \Omega$. It is suggested that the uniformity of the sensitivity field also decreases when parasitic resistance is present.

3.1.3. Evaluation of parasitic resistance under different background conductivities. The above analysis show that parasitic resistance influences the measurement current and sensitivity distribution to a certain degree. Therefore, the influence of parasitic resistance with respect to different background conductivities was quantitatively evaluated.

Table 3. Value of *CD* under different models.

Model 1: R_p	1×10^{-1} S m^{-1}	1×10^{-2} S m^{-1}	1×10^{-3} S m^{-1}	1×10^{-4} S m^{-1}	1×10^{-5} S m^{-1}
300 Ω	80.46%	79.16%	25.63%	6.11%	4.27%
30 Ω	74.44%	25.16%	3.51%	0.63%	0.43%
3 Ω	24.81%	3.45%	0.36%	0.17%	0.043%
0.3 Ω	3.12%	0.33%	0.033%	0.0057%	0.0042%
Model 2: R_p	1×10^{-1} S m^{-1}	1×10^{-2} S m^{-1}	1×10^{-3} S m^{-1}	1×10^{-4} S m^{-1}	1×10^{-5} S m^{-1}
300 Ω	104.85%	147.13%	65.39%	14.30%	9.49%
30 Ω	158.38%	63.93%	8.78%	1.42%	0.93%
3 Ω	69.45%	8.60%	0.89%	0.14%	0.097%
0.3 Ω	8.56%	0.81%	0.093%	0.0013%	0.0098%

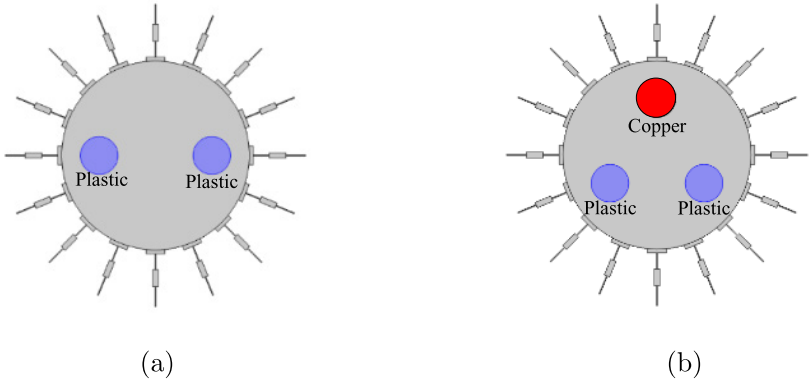

Figure 6. Simulation model: (a) phantom 3, (b) phantom 4.

As shown in table 2, the plastic rods (diameter 20 mm, conductivity 1×10^{-12}S m^{-1}) were placed in the sensing field (diameter 100 mm) and the measurement currents were collected. In each figure, the y-coordinate of the curve is the difference in the measurement current calculated by

$$\Delta I = (I_x - I_e)/I_e \tag{11}$$

where I_e is the measurement current when the sensing field is filled with background conductive material and I_x is the measured current when a conductivity perturbation, i.e. a plastic rod, is inserted in the sensing field.

In order to quantitatively describe the influence of parasitic resistance on the measurement results, the value of the criterion *CD* was proposed, which was calculated by

$$CD = \frac{||\Delta I_{Rp} - \Delta I||}{||\Delta I||} \times 100\% \tag{12}$$

where ΔI_{Rp} and ΔI are the normalized measurement currents under the model with and without parasitic resistance, respectively.

The criterion *CD* represents the influence of parasitic resistance on the measurement results. The influence decreases as *CD* becomes small.

The results in table 2 show that the influence of background conductivity on the measurement current varies with the different parasitic resistances. In these figures, the black curve indicates the case of $Rp = 0$ Ω. As the background conductivity decreases, the measurement current curve approximates to the black curve, indicating that the parasitic resistance has less influence on the measurement current. Table 3 lists the quantitative results. Moreover, it can be seen that the sensor with $R_p = 0.3$ Ω is very similar to that with $R_p = 0$ Ω, thus the condition of $R_p = 0.3$ Ω will not be considered in the following studies.

In order to evaluate the quality of the reconstructed images, the correlation coefficient (*CC*) [35] between the actual conductivity distribution and the reconstructed distribution was calculated, i.e.

$$CC = \frac{\sum_{i=1}^{N_p} (g_i - \bar{g})(\hat{g}_i - \bar{\hat{g}})}{\sqrt{\sum_{i=1}^{N_p} (g_i - \bar{g})^2 \sum_{i=1}^{N_p} (\hat{g}_i - \bar{\hat{g}})^2}} \tag{13}$$

where g is the conductivity vector of the real distribution, $\hat{g}$ is the conductivity vector of the reconstructed image, $\bar{g}$ and $\bar{\hat{g}}$ are the mean values of g and $\hat{g}$, respectively, and N_p is the number the pixels in the imaging area.

The reconstructed images of the model shown in figure 6 using the LBP algorithm are listed in tables 4 and 5.

It can be found from tables 4 and 5 that the reconstructed image clearly reflects the actual distribution as parasitic resistance decreases. Moreover, the influence of parasitic resistance

Table 4. The reconstructed image of phantom 3 under different background conductivities.

R_p \ σ_w	1×10^{-1} S m^{-1}	1×10^{-2} S m^{-1}	1×10^{-3} S m^{-1}	1×10^{-4} S m^{-1}	1×10^{-5} S m^{-1}
300 Ω	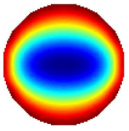 $CC = 0.2727$	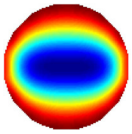 $CC = 0.3239$	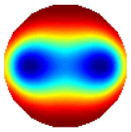 $CC = 0.4859$	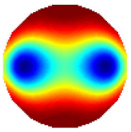 $CC = 0.5584$	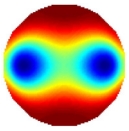 $CC = 0.5666$
30 Ω	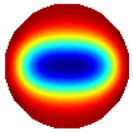 $CC = 0.2716$	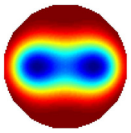 $CC = 0.4586$	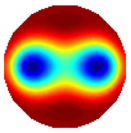 $CC = 0.5633$	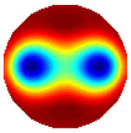 $CC = 0.5780$	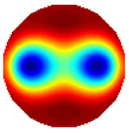 $CC = 0.5795$
3 Ω	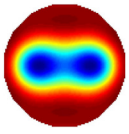 $CC = 0.4274$	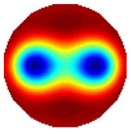 $CC = 0.5399$	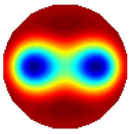 $CC = 0.5566$	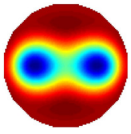 $CC = 0.5583$	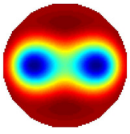 $CC = 0.5585$
0 Ω	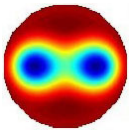 $CC = 0.5519$	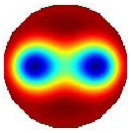 $CC = 0.5537$	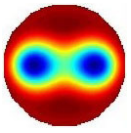 $CC = 0.5839$	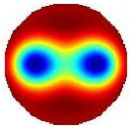 $CC = 0.5839$	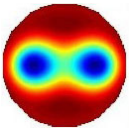 $CC = 0.5839$

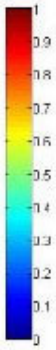

becomes smaller as the background conductivity decreases when parasitic resistance remains unchanged.

In order to quantitatively evaluate the results, the index *re* is introduced:

$$re = \frac{CC}{CC_{\max}} \times 100\% \tag{14}$$

where $CC_{\max}$ is the maximum correlation coefficient under different background conductivities with $R_p = 0$.

The index *re* indicates that relationship of correlation coefficients between the two cases. The influence of parasitic resistance on the reconstructed images becomes smaller with increase in the index *re*. In this paper, the influence of parasitic resistance on reconstructed images can be ignored when *re* is greater than 90%. The *re* values calculated with the two models are listed in tables 6 and 7 and images of the values are shown in figure 7.

It can be seen from figure 7 that the value of *re* increases as the background conductivity decreases, suggesting that the parasitic resistance has less influence on the reconstructed image as the conductivity decreases. The different curves show different values of background conductivity when $re = 90\%$. It has been suggested that this critical value of background conductivity decreases as the parasitic resistance increases.

In order to further evaluate the influence of R_p on the reconstructed images under different background conductivities, the parameter k_r has been proposed, which can be calculated by

$$k_r = R_p \sigma_w. \tag{15}$$

The value of k_r under different parasitic resistances and background conductivities is shown in table 8.

As can be seen from figure 8, the values of k_r in the two phantoms are both smaller than 3×10^{-2} when $re = 90\%$. That is, in the above simulation, the parasitic resistance has little impact on the reconstructed image when the value of k_r is smaller than 3×10^{-2}. From this result, the applicable range of background conductivity can be found according to table 8 when the parasitic resistance is known.

However, the above study was only established under a fixed sensor structure, without considering the influence of other structural parameters on the results. Therefore, we propose a parameter S_P, which is defined by

$$S_P = \frac{\text{width} \times \text{number}}{\text{diameter}} \tag{16}$$

where width and number stand for the width and the number of electrodes, respectively, and *diameter* stands for the diameter of the sensing field.

The purpose of the following study is to find out the relationship between k_r and *re* under different values of S_P, as shown in table 9.

The simulation model is established according to different structural parameters shown in table 9. Then the curves for the relationship between *kr* and *re* in the simulation models are drawn as shown in figure 9.

Table 5. The reconstructed image of phantom 4 under different background conductivities.

R_p \ σ_w	1×10^{-1} S m^{-1}	1×10^{-2} S m^{-1}	1×10^{-3} S m^{-1}	1×10^{-4} S m^{-1}	1×10^{-5} S m^{-1}
300 Ω	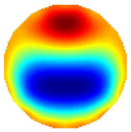 $CC = 0.3300$	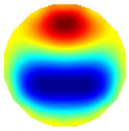 $CC = 0.3775$	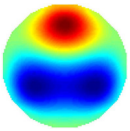 $CC = 0.4401$	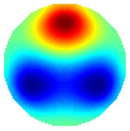 $CC = 0.4594$	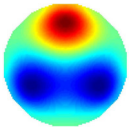 $CC = 0.4618$
30 Ω	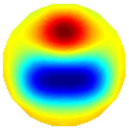 $CC = 0.3645$	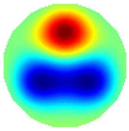 $CC = 0.4434$	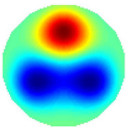 $CC = 0.4754$	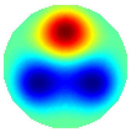 $CC = 0.4801$	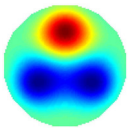 $CC = 0.4806$
3 Ω	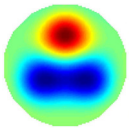 $CC = 0.4257$	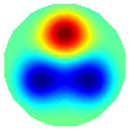 $CC = 0.4637$	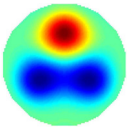 $CC = 0.4696$	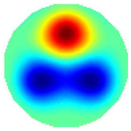 $CC = 0.4703$	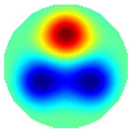 $CC = 0.4703$
0 Ω	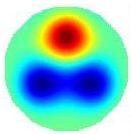 $CC = 0.4873$	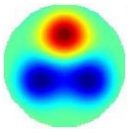 $CC = 0.4877$	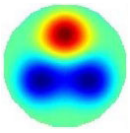 $CC = 0.4877$	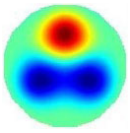 $CC = 0.4877$	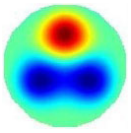 $CC = 0.4877$

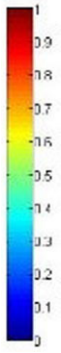

Table 6. The value of *re* in phantom 3.

R_p \ σ_w	1×10^{-1} S m^{-1}	1×10^{-2} S m^{-1}	1×10^{-3} S m^{-1}	1×10^{-4} S m^{-1}	1×10^{-5} S m^{-1}
300 Ω	46.70%	55.47%	83.22%	95.63%	97.04%
30 Ω	46.51%	78.54%	96.47%	98.99%	99.25%
3 Ω	73.20%	92.46%	95.32%	95.62%	95.65%

Table 7. The value of *re* in phantom 4.

R_p \ σ_w	1×10^{-1} S m^{-1}	1×10^{-2} S m^{-1}	1×10^{-3} S m^{-1}	1×10^{-4} S m^{-1}	1×10^{-5} S m^{-1}
300 Ω	67.66%	77.40%	90.24%	94.20%	94.69%
30 Ω	74.74%	90.92%	97.48%	98.44%	98.54%
3 Ω	87.29%	95.08%	96.29%	96.43%	96.43%

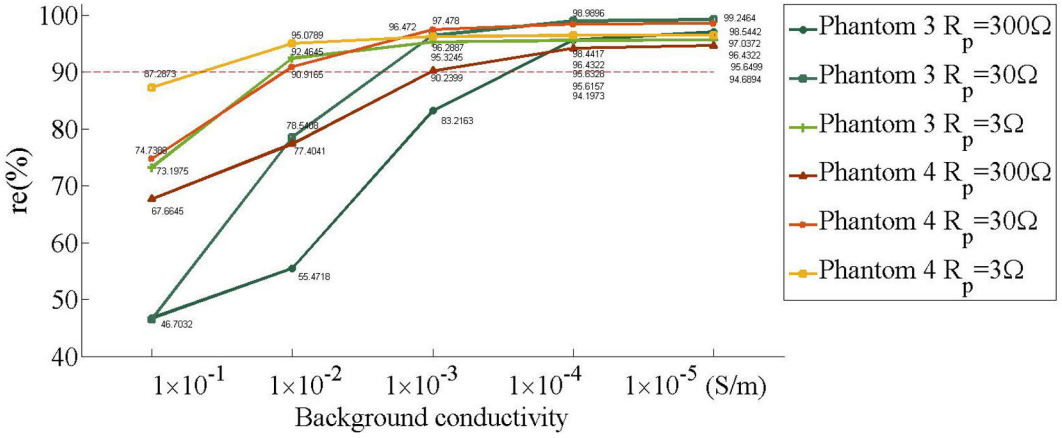

Figure 7. The value of *re* in phantom 3 and 4.

Table 8. The value of k_r.

R_p \ σ_w	1×10^{-1} S m^{-1}	1×10^{-2} S m^{-1}	1×10^{-3} S m^{-1}	1×10^{-4} S m^{-1}	1×10^{-5} S m^{-1}
300 Ω	30	3	3×10^{-1}	3×10^{-2}	3×10^{-3}
30 Ω	3	3×10^{-1}	3×10^{-2}	3×10^{-3}	3×10^{-4}
3 Ω	3×10^{-1}	3×10^{-2}	3×10^{-3}	3×10^{-4}	3×10^{-5}

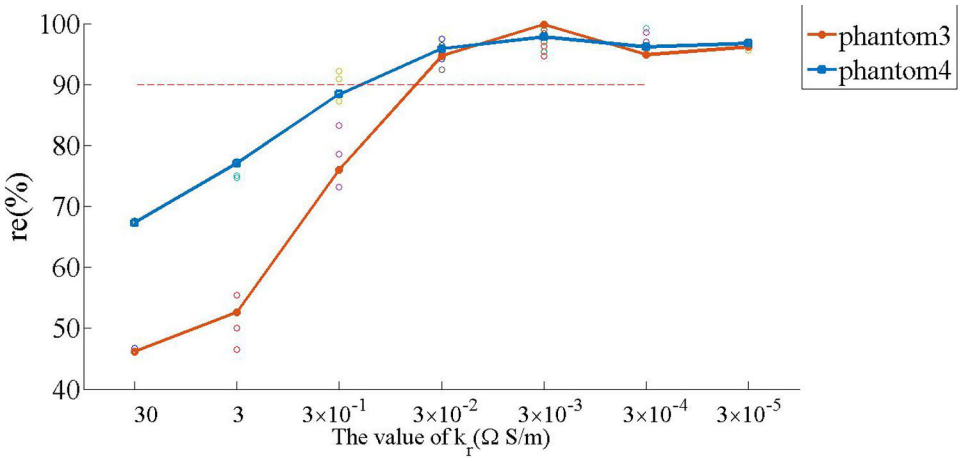

Figure 8. The relationship between k_r and *re* in phantoms 3 and 4.

It can be seen from figure 9 that all the values of k_r fluctuate around 3×10^{-2} when $re = 90\%$, under different values of S_P. These results are similar to those of the previous study. It can be suggested that the influence of structural parameters S_P on the value of k_r is small and can be ignored when studying the relationship between k_r and the background conductivity. Therefore, the above results can be generalized to different structures. That is, when the value of k_r is smaller than 3×10^{-2} the parasitic resistance has little impact on the reconstructed image. Moreover, the applicable range of background conductivity can be found according to table 8 when the parasitic resistance of the system is known.

3.2. Experiments

3.2.1. Measurement system. The measurement system is implemented using a commercial LCR meter (Keysight E4980AL) and a custom-built analog switch array, which is controlled by an Arduino Nano MCU as shown in figure 10.

The switch array was implemented by a CMOS analog switch device (DG413). Figure 11 shows the equivalent circuit for each channel.

Prior to the experiments, the parasitic resistances in each channel, including the ON-resistance and wire resistance, were collected by the LCR meter; these are listed in table 10. The results show that the parasitic resistance in each channel fluctuates around 31 Ω.

3.2.2. Current measurements and image reconstruction. Preliminary measurements were collected with the ERTv measurement system to verify the simulation results. It is known that the parasitic resistance of this system is 31 Ω. The parasitic resistance has little impact on the reconstructed image when k_r is smaller than 3×10^{-2}. At this point, the conductivity should be less than 1×10^{-3} S m^{-1}, according to table 8. The effect on the reconstructed images in this range is verified below.

Table 9. Parameters for different values of S_P.

S_P	Diameter (mm)	Number	Width (mm)
0.80	300	12	20
1.00	80	8	10
1.60	500	16	50
2.88	100	8	36

The conductivity of water, from 6.23×10^{-4} S m^{-1} to 1.24 S m^{-1}, was controlled by the addition of salt. Table 11 shows the curves of current measurements under different background conductivities. It shows the same variational trend as the simulation results. The dynamic range of the measurement currents becomes larger as the background conductivity decreases.

Table 12 shows image reconstruction of data sets under different conductivity distributions. The black rings in each reconstructed image indicate the location of the non-conductive rods. Image reconstruction was performed with the LBP algorithm.

As indicated in the numerical simulations, when the conductivity of the water increases the effect of parasitic resistance becomes more significant. The impact of measurement errors is increased for water with a high conductivity. This

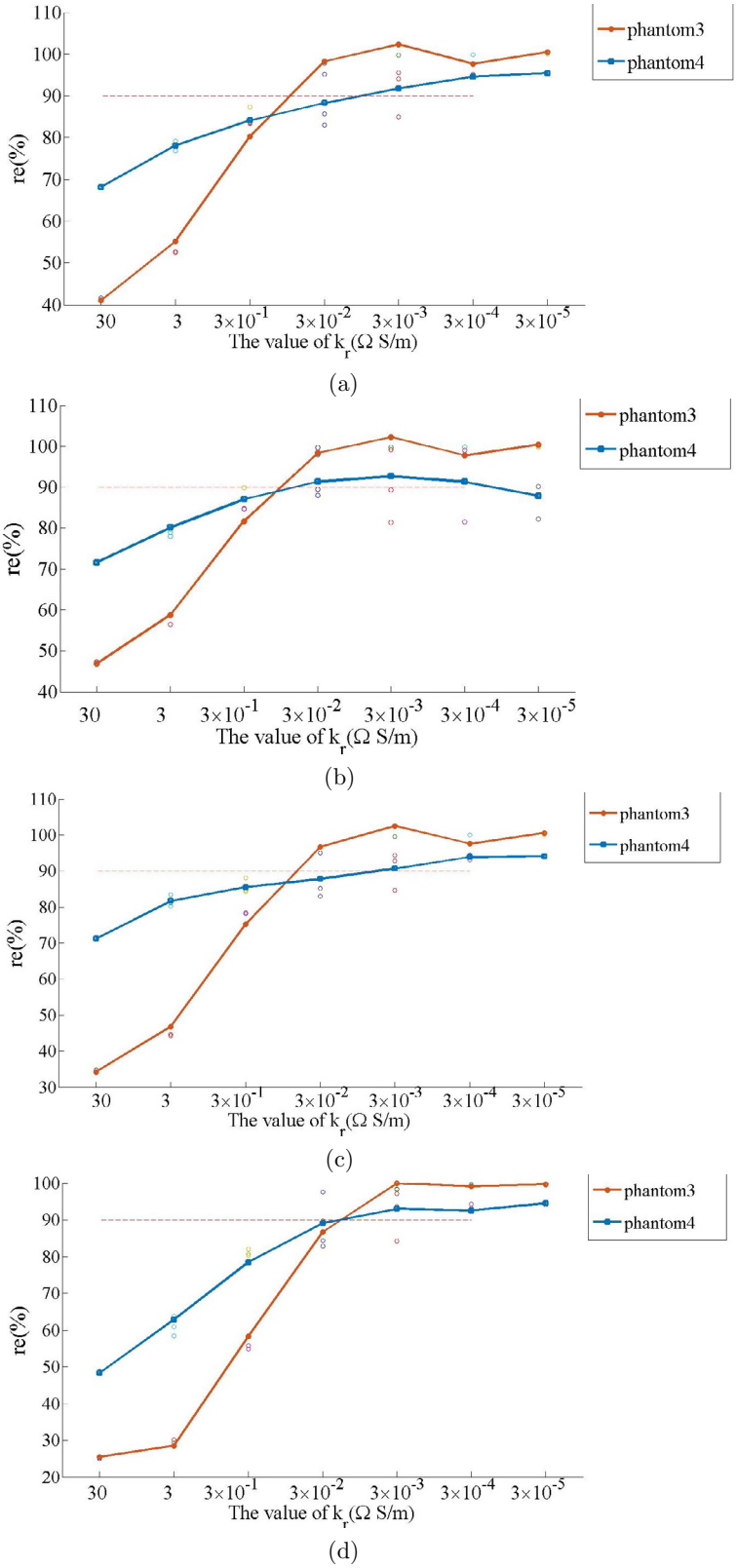

Figure 9. The relationship between k_r and *re* under different S_P.

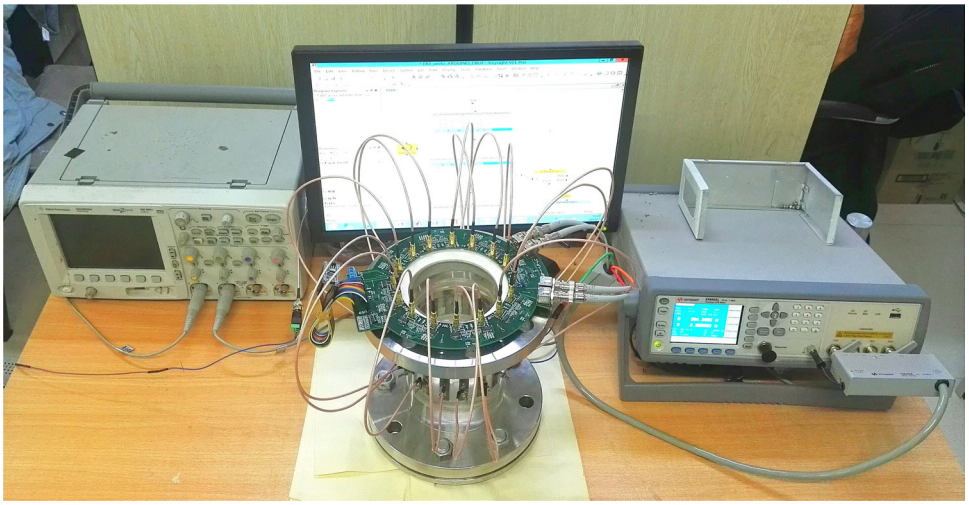

Figure 10. ERTv system with an LCR meter.

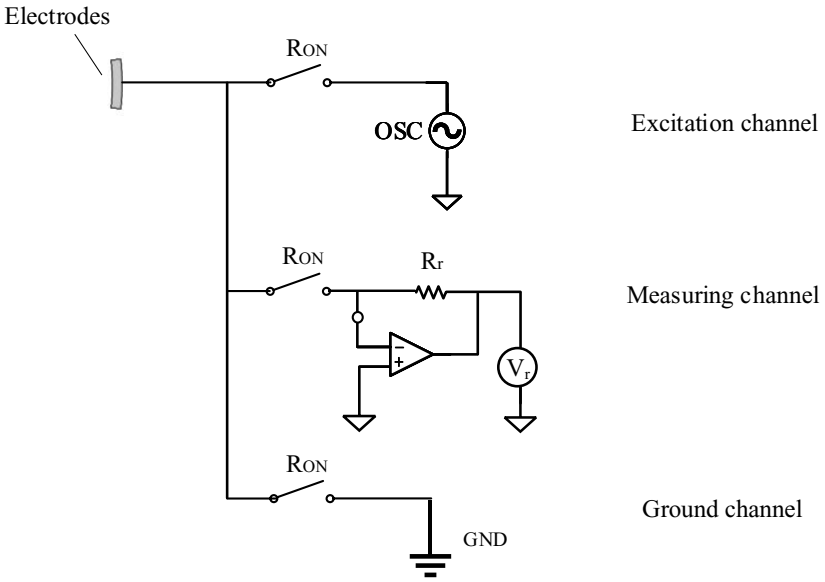

Figure 11. Switch connection of each electrode.

Table 10. The actual measurement of parasitic resistance.

parasitic resistance	Maximum	Minimum	Mean	Variance
R_{p1}	31.2 Ω	30.6 Ω	30.9938 Ω	0.0273
R_{p2}	31.3 Ω	30.8 Ω	31.0062 Ω	0.0206
R_{p3}	31.2 Ω	30.8 Ω	31.0250 Ω	0.0220

is because the values of inter-electrode resistance are comparable in the magnitude to the parasitic resistance.

The experimental results are consistent with the simulations. As can be seen from the reconstructed images, the gaps between the rods can be better observed when the background conductivity is less than 6.7×10^{-3} S m^{-1}. Under this circumstance, the reconstructed images can better represent the actual distribution according to the parameters *CC*, *re* and *kr*. The conductivity range is very close to that deduced from *kr*, which verifies the feasibility of the method.

Table 11. The current curves under different background conductivities.

Phantom		
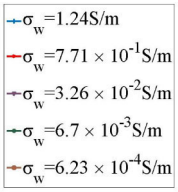	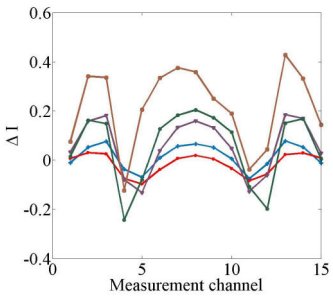	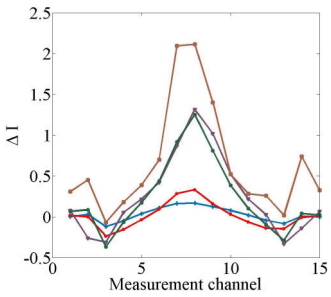

Table 12. The experiment results under different background conductivities.

	$1.24\,\mathrm{S\ m^{-1}}$	$7.71\times10^{-1}\,\mathrm{S\ m^{-1}}$	$3.26\times10^{-2}\,\mathrm{S\ m^{-1}}$	$6.7\times10^{-3}\,\mathrm{S\ m^{-1}}$	$6.23\times10^{-4}\,\mathrm{S\ m^{-1}}$
Phantom	Saline water		Tap water		Distilled water
	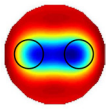	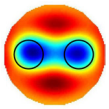	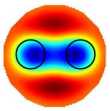	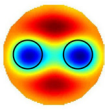	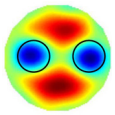
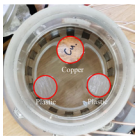	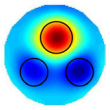	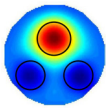	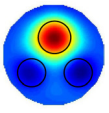	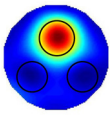	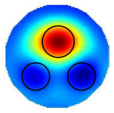

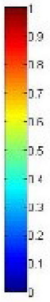

4. Conclusions

In the ERTv system, the presence of parasitic resistance in each measurement channel will inevitably affect the measurements and image results. In order to evaluate this effect, the measurements and the sensitivity distributions of an ERTv system have been analyzed and compared, taking the parasitic resistance into consideration. Generally, the impact of parasitic resistance depends on the background conductivity to a great extent. Therefore, a series of numerical and experimental studies were carried out to quantitatively evaluate the effect of parasitic resistance. The parasitic resistance is generally in the range between 0.1 and 100 Ω.

In the case of parasitic resistance no greater than 30 Ω, the ERTv system can be directly applied to fluids dominated by tap water (typical conductivity $1\times10^{-2}\,\mathrm{S\ m^{-1}}$). However, if the background conductivity of investigated fluids is greater than $1\times10^{-2}\,\mathrm{S\ m^{-1}}$, i.e. sea water, the parasitic resistance should be limited to less than 3 Ω. In addition, a criterion for determining the applicable background conductivity for different parasitic resistances has been suggested. If the value of parasitic resistance R_p of the ERTv system is given, the background conductivity of investigated fluids should be within the range listed in table 8. It is recommended that the criterion k_r should be no greater than 3×10^{-2}.

In this research, the average parasitic resistance of the ERTv system is 31.0083 Ω. Therefore, the background conductivity applicable to this system is less than $1\times10^{-3}\,\mathrm{S\ m^{-1}}$. It can be found in the experiments that the reconstructed image can better reflect the conductivity distribution of the phantom when the background conductivity is less than $6.7\times10^{-3}\,\mathrm{S\ m^{-1}}$. It can be concluded that parasitic resistance can be readily neglected when the criterion $k_r \leqslant 3\times10^{-2}$ can be satisfied.

Acknowledgment

The authors are grateful for financial support from National Natural Science Foundation of China (Grant Nos. 61627803, 61671319).

ORCID iDs

Chao Wang https://orcid.org/0000-0002-4362-947X
Qingqing Cao https://orcid.org/0000-0001-6329-8746
Ziqiang Cui https://orcid.org/0000-0003-0498-9955

References

[1] Kourunen J, Niitti T and Heikkinen L M 2011 Application of three-dimensional electrical resistance tomography to characterize gas holdup distribution in laboratory flotation cell *Miner. Eng.* **24** 1677–86

[2] Razzak S A, Barghi S, Zhu J X and Mi Y 2009 Phase holdup measurement in a gas–liquid–solid circulating fluidized bed (GLSCFB) riser using electrical resistance tomography and optical fibre probe *Chem. Eng. J.* **147** 210–8

[3] Jin H, Han Y, Yang S and He G 2010 Electrical resistance tomography coupled with differential pressure measurement to determine phase hold-ups in gas–liquid–solid outer loop bubble column *Flow Meas. Instrum.* **21** 228–32

[4] Wang M 2005 Seeing a new dimension—the past decade's developments on electrical impedance tomography *Prog. Nat. Sci.* **15** 1–13

[5] Razzak S A, Barghi S and Zhu J X 2007 Electrical resistance tomography for flow characterization of a gas–liquid–solid three-phase circulating fluidized bed *Chem. Eng. Sci.* **62** 7253–63

[6] Ross A S, Saulnier G J, Newell J C and Isaacson D 2003 Current source design for electrical impedance tomography *Physiol. Meas.* **24** 509–16

[7] Cardu R, Leong P H W, Jin C T and McEwan A 2012 Electrode contact impedance sensitivity to variations in geometry *Physiol. Meas.* **33** 817–30

[8] Brown B H and Seagar A D 1987 The Sheffield data collection system *Clin. Phys. Physiol. Meas.* **8** 91–7

[9] Gisser D G, Isaacson D and Newell J C 1987 Current topics in impedance imaging *Clin. Phys. Physiol. Meas.* **8** 39–46

[10] Woo E J, Hua P, Webster J G and Tompkins W J 1992 Measuring lung resistivity using electrical impedance tomography *IEEE Trans. Biomed. Eng.* **39** 756–60

[11] Chen J, Xu L, Cao Z and Zhou H 2014 Four-terminal imaging using a two-terminal electrical impedance tomography system *IEEE Trans. Instrum. Meas.* **63** 432–40

[12] Olerni C, Jia J and Wang M 2013 Measurement of air distribution and void fraction of an upwards air–water flow using electrical resistance tomography and a wire-mesh sensor *Meas. Sci. Technol.* **24** 035403

[13] Rafiei-Naeini M and McCann H 2008 Low-noise current excitation sub-system for medical EIT *Physiol. Meas.* **29** 173–84

[14] Sun J and Yang W 2014 Evaluation of fringe effect of electrical resistance tomography sensor Measurement **53** 145–60

[15] Sun J and Yang W 2013 Fringe effect of electrical capacitance and resistance tomography sensors *Meas. Sci. Technol.* **24** 464–75

[16] Jia J, Wang M and Schlaberg H I 2010 A novel tomographic sensing system for high electrically conductive multiphase flow measurement *Flow Meas. Instrum.* **21** 184–90

[17] Frias M A R and Yang W 2016 Electrical resistance tomography with voltage excitation *Conf. Proc. IEEE International Instrumentation and Measurement Technology* pp 1–6

[18] Wang R, Frias M A R, Wang H, Yang W and Ye J 2018 Evaluation of electrical resistance tomography with voltage excitation compared with electrical capacitance tomography *Meas. Sci. Technol.* **29** 125401

[19] Cui Z, Wang H, Xu Y and Fan W 2010 Design of twin-plane electrical resistance tomography system *J. Tianjin Univ.* **43** 115–20

[20] Mao M, Ye J, Wang H, Zhang J and Yang W 2016 Evaluation of excitation strategy with multi-plane electrical capacitance tomography sensor *Meas. Sci. Technol.* **27** 114008

[21] Sun J and Yang W 2015 A dual-modality electrical tomography sensor for measurement of gas–oil–water stratified flows *Measurement* **66** 150–60

[22] Saulnier G J, Ross A S and Liu N 2006 A high-precision voltage source for EIT *Physiol. Meas.* **27** S221

[23] Malmivuo J and Plonsey R 1995 *Bioelectromagnetism: Principles and Applications of Bioelectric and Biomagnetic Fields* (vol 1) (Rome: Societa Editrice Il Foro Italiano ARL)

[24] Frias M A R and Yang W 2017 Effect of parasitic resistance in electrical resistance tomography with voltage excitation *2017 IEEE Int. Conf. on Imaging Systems and Techniques* (https://doi.org/10.1109/IST.2017.8261552)

[25] Rodriguez-Frias M A and Yang W Sensor design for four-electrode electrical resistance tomography with voltage excitation *IEEE Sensors J.* **2019** 1

[26] Wang H 2013 *Electrical Tomography* (Beijing: Science Press)

[27] Feng C and Ma X 2013 *Introduction to Engineering Electromagnetic Fields* (Beijing: Higher Education Press)

[28] Boyle A and Adler A 2011 The impact of electrode area, contact impedance and boundary shape on EIT images *Physiol. Meas.* **32** 745–54

[29] Xie C G, Huang S M, Hoyle B S, Thorn R, Lenn C, Snowden D, Beck M S, Xie C G, Huang S M and Hoyle B S 1992 Electrical capacitance tomography for flow imaging: system model for development of image reconstruction algorithms and design of primary sensors *Circuits Devices Syst. IEE Proc. G* **139** 89–98

[30] Lehr J 1972 A vector derivation useful in impedance plethysmographic field calculations *IEEE Trans. Biomed. Eng.* **19** 156–7

[31] Dong F, Liu X P, Deng X and Ling an X U 2001 Application of electrical resistance tomography to two-phase pipe flow measurement *Control Instrum. Chem. Ind.* **14** 183–92

[32] Ye J, Wang H and Yang W 2014 A sparsity reconstruction algorithm for electrical capacitance tomography based on modified Landweber iteration *Meas. Technol.* **25** 115402

[33] Qiang G, Meng S, Wang D, Zhao Y and Liu Z 2017 Investigation of gas–solid bubbling fluidized beds using ECT with a modified Tikhonov regularization technique *AICHE J.* **64** 29–41

[34] Hua-Xiang *et al* 2008 Optimal design of ERT/ECT dual-modality sensing electrode array *J. Tianjin Univ.* **8** 911–8

[35] Xie C, Huang S, Lenn C and Stott A L 1994 Experimental evaluation of capacitance tomographic flow imaging systems using physical models *IEE Proc.* **141** 357–68